High-Resolution Microwave Photonic Radar With Sparse Stepped Frequency Chirp Signals

Cong Ma, Yue Yang, Fengting Cao, Xiangchuan Wang, Xi Liu, Chenkai Meng, Jiangtao Zhang, and Shilong Pan, *Senior Member, IEEE*

***Abstract*— High-resolution radar requires broadband signal generation and processing, which challenges the state-of-the-art electronics. In contrast, microwave photonic technologies featuring wide bandwidth and flexible frequency are effective for broadband microwave signal generation and processing to improve radar detection performance. However, the bandwidth is practically limited because the broadband radar with a continuous spectrum signal is always susceptible to interference from other electromagnetic applications operating at the coincident frequency band. Here, we propose a microwave photonic radar with sparse stepped frequency chirp (SSFC) signals to break through the bandwidth limitation, achieving ultrahigh-resolution detection with enhanced anti-interference ability. The SSFC signal with an ultrawide bandwidth is generated by recirculating frequency-shifting a narrowband chirp signal. Microwave photonic dechirping of SSFC signals and compressive reconstructions of dechirped signals are performed to extract target information fast and precisely. In the experiment, we conducted a microwave photonic radar based on an SSFC signal spanning a frequency range of 18 GHz but actually occupying a 4.5-GHz effective spectrum, successfully distinguishing two simulated point targets with a distance of 8.3 mm, and achieving the ranging error within ±225 μm. In addition, high-precision vibration monitoring and high-resolution two-dimensional imaging capabilities are validated by a simple pendulum detection and an inverse synthetic aperture radar (ISAR) experiment.**

***Index Terms*— High resolution, microwave photonics, radar, sparse stepped frequency chirp (SSFC) signals.**

I. INTRODUCTION

HIGH-RESOLUTION microwave radar, including synthetic aperture radar (SAR) and inverse SAR (ISAR), as an all-day and all-weather sensor is highly demanded in many applications, such as target recognition, remote sensing, and environmental surveillance [1], [2], [3]. However, the wide bandwidth waveform generation and processing challenge the state-of-the-art electronics to achieve high-resolution detection. For example, the direct digital synthesizer (DDS)-based electronic frequency synthesizer usually utilized in the conventional radar suffers from a limited bandwidth of a few gigahertz [4]. To produce a larger bandwidth waveform based on electronic technologies, multiple frequency converters and multipliers are generally necessary, leading to some inevitable spurious signals [5]. Besides, the broadband radar signal is difficult to be directly processed due to the low-speed limit of electronic analog-to-digital converters (ADCs). In the past years, microwave photonics featuring wide bandwidth, low transmission loss, and immunity to electromagnetic interference has received increased attention [6], [7], [8]. Especially, microwave photonics can present remarkable performance compared with electronics for broadband signal generation and processing. In terms of signal generation, optical heterodyne, photonic frequency multiplication, photonic digital-to-analog converter (DAC), optoelectronic oscillator (OEO), and so on can easily produce broadband radar waveforms [9], [10], [11], [12], while with regard to broadband signal processing, photonic sampling, photonic Fourier transformation, photonic frequency mixing, and so on enable fast or even real-time processing [13], [14], [15]. Integrating the aforementioned technologies into radars, the detection performance would be significantly improved [16], [17], [18], [19], [20].

As early as 2014, microwave photonic radar based on frequency-to-time mapping (FTM) was proposed, which can produce tens of gigahertz bandwidth signals to achieve millimeter-level range resolution [21], showing the outstanding wideband performance of microwave photonics. The major obstacle to the practical application of FTM-based schemes is the small time-bandwidth product (TBWP) limited by its short duration, which leads to a low power density that is not suitable for remote detection. In the same year, a more realistic solution based on a passive mode-locked laser (MLL) was demonstrated, showing the advantages of extreme frequency flexibility compared with the conventional electronic radar [22]. However, the bandwidth of the radar waveform is limited by the low repetition frequency of the passive MLL, resulting in a finite range resolution of about several meters. Although an active MLL can be used to increase the repetition frequency, the bandwidth of the radar waveform is still restricted by the electrical signal generator (ESG) [23]. To alleviate the demand for broadband ESGs, microwave photonic frequency multipliers could be employed for broadband signal generation. Furthermore, real-time high-resolution radar imaging could be realized combined with microwave photonic

Manuscript received 1 June 2022; revised 10 August 2022; accepted 16 September 2022. Date of publication 20 September 2022; date of current version 14 October 2022. This work was supported in part by the National Natural Science Foundation of China under Grant 62075095, in part by the Young Elite Scientists Sponsorship Program by CAST under Grant 2018QNRC001, in part by the Key Research and Development Program of Jiangsu Province under Grant BE2020030. *(Corresponding authors: Xiangchuan Wang; Shilong Pan.)*

The authors are with the Key Laboratory of Radar Imaging and Microwave Photonics, Ministry of Education, Nanjing University of Aeronautics and Astronautics, Nanjing 210016, China (e-mail: wangxch@nuaa.edu.cn; pans@nuaa.edu.cn).

Digital Object Identifier 10.1109/TGRS.2022.3208112

dechirping [24], [25], [26]. Field experiments indicate that the radar based on microwave photonic frequency multiplication and dechirping, whether on the ground or airborne platforms, has the feasibility of detecting both weak and strong targets [27], [28], [29]. Nevertheless, it still requires the support of a broadband ESG to generate a waveform with an ultrawide bandwidth to achieve ultrahigh resolution. More than that, due to the scarcity of radio spectrum resources, the broadband signal with a continuous spectrum is usually susceptible to radio spectrum pollution from other electromagnetic equipment, thus limiting the practical use of broadband signals. To reduce external electromagnetic interference, broadband signals in multiple bands spectra can be used in microwave photonic radar. For example, coherent radar operating in multiple bands has been developed due to the wide spectrum of the MLL [30]. However, radar signals in different bands should be separated by sharp and narrow filters, which is a challenge in practice. In addition, to achieve high-resolution detection, multiple parallel transceivers are required, thus inevitably increasing system costs. Apart from MLL-based schemes, microwave photonic dual-band radars based on the FTM [31], microwave photonic frequency multiplication [32], and photonic DAC [33] have been explored. Among them, the radars based on FTM and frequency multiplication have similar limitations as the aforementioned continuous spectrum radar based on the same scheme, while the performance of the photonic DAC-based radar is also limited by the low bit rate and low effective number of bits (ENOB) of the ESG.

Different from the way taken by multiband radar, it can also directly employ signals with a sparse spectrum, such as stepped frequency (SF) signal or stepped frequency chirp (SFC) signal to avoid electromagnetic interference [34], [35], [36]. Here, the sparse spectrum refers to a series of discontinuous frequencies. The SF signal not only significantly reduces the instantaneous bandwidth requirement of the transceiver but also improves the anti-jamming capability of the radar. Until recently, a microwave photonic radar based on an SF signal has been proven to achieve a centimeter-level spatial resolution [37]. However, the SF-based radar's unambiguous range is limited by frequency steps. In addition, the SF signal is sensitive to the radial velocity of the target, which leads to complex range-Doppler coupling [38]. In contrast to the SF signal, the SFC signal can significantly suppress range ambiguity and can be processed quickly by dechirping like the chirp signal. Utilizing the broadband SFC signal generated based on an optical frequency shifting loop (OFSL), we have demonstrated a high-resolution imaging radar [39]. Nevertheless, the above microwave photonic radars mainly considered SF and SFC signal with a continuous spectrum, where the bandwidth is still practically limited due to interferences.

More recently, we have reported a novel microwave photonic radar based on an SFC signal with a sparse spectrum and verified its feasibility through a simple ranging experiment [40]. In this article, we further propose and demonstrate a microwave photonic radar with a sparse SFC (SSFC) signal aiming to break through the bandwidth limitation caused by electronic implementations and electromagnetic interference. In the transmitter, the SSFC signal with a wide bandwidth is

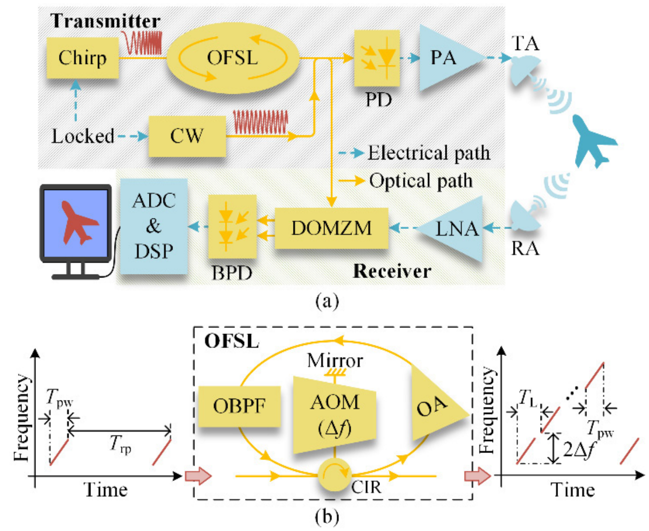

Fig. 1. (a) Configuration of the proposed radar. (b) Schematic of the OFSL. OFSL, PD, PA, TA, RA, LNA, DOMZM, BPD, ADC, DSP, OBPF, AOM, OA, and CIR.

produced due to recirculating frequency shift implemented by an on OFSL based on an acousto-optic modulator (AOM). Compared with the dual-parallel Mach–Zehnder modulator (DP-MZM)-based OFSL [39], the stability of the AOM-based method is improved because the half-wave voltage of the DP-MZM is susceptible to environmental disturbances, which deteriorates the harmonic rejection ratio of the generated signal. Benefiting from the sparse spectrum spanning a wide bandwidth, the SSFC signal can not only carry target information with more details but also improve the anti-interference ability of the radar. In the receiver, microwave photonic dechirping is adopted to convert the broadband SSFC signal to a low-frequency dechirped signal, which can be digitized by a low-speed ADC. In addition, a compressive reconstruction of the dechirped signal is implemented to extract target information precisely. In the experiments, a microwave photonic radar with a working bandwidth of up to 18 GHz and an actually occupied spectrum of 4.5 GHz is established, enabling a subcentimeter range resolution and submillimeter ranging precision. In addition, a simple pendulum is detected to verify the high-precision vibration monitoring capability, while an ISAR is designed to verify the high-resolution imaging capability.

II. Principle

A. System Configuration

Fig. 1(a) presents the schematic of the proposed microwave photonic radar with an SSFC signal. In the transmitter, a narrow bandwidth frequency-chirped light with a center frequency of f_{Lc} and bandwidth of B_L, as a seed light source, is sent to an OFSL, which is the core of the transmitter to perform recirculating frequency shift. As shown in Fig. 1(b), the main components of the OFSL include a circulator (CIR), an AOM, a Faraday mirror, an optical amplifier (OA), and an optical bandpass filter (OBPF). The frequency-chirped light propagates through the AOM twice in a round trip after being reflected by the Faraday mirror. Assuming the frequency shift of the AOM is Δf, the frequency of the light in the loop will be shifted by $2\Delta f$ during the round trip. By setting the power gain of the OA to be equal to the power loss of OFSL, i.e., the open-loop gain is 1, the frequency of the light in the loop will be shifted round by round. Furthermore, taking into account the radar detection scenario in practice, the bandwidth of the generated radar signal can be adjusted by controlling the cutoff frequency of the OBPF in the OFSL to regulate the maximum frequency-shift number $N_{\max}$: $N_{\max} = \lfloor (f_{\mathrm{Hcut}} - f_{\mathrm{Lc}} - B_{\mathrm{L}}/2)/(2\Delta f) \rfloor$, where f_{Hcut} is the high cutoff frequency of the OBPF and $\lfloor x \rfloor$ denotes the largest integer no more than x. Moreover, the low cutoff frequency f_{Lcut} of the OBPF should be lower than $f_{\mathrm{Lc}} + 2\Delta f - B_{\mathrm{L}}/2$ to allow the seed light source to be injected into the OFSL smoothly. Consequently, an optical SFC signal output from the OFSL can be written as

$$E_{\mathrm{OFSL}}(t) = E_{\mathrm{OSFC}} \sum_{k=0}^{N_{\max}-1} \mathrm{rect}\left(\frac{t-kT_{\mathrm{L}}}{T_{\mathrm{pw}}}\right) \cdot \exp\left[j\{2\pi[f_{\mathrm{Lc}} + 2(k+1)\Delta f + \gamma(t-kT_{\mathrm{L}})/2] \times (t-kT_{\mathrm{L}}) + \varphi_k\}\right] \quad (1)$$

where E_{OSFC} denotes the amplitude of the output optical SFC signal, $\mathrm{rect}(x) = \{1, |x| \le 0.5;\ 0, |x| > 0.5\}$, $\gamma = B_{\mathrm{L}}/T_{\mathrm{pw}}$ is the chirp rate, T_{pw} and T_{L} are the pulsewidth of the seed light source and the circulation time of the OFSL, and φ_k is the initial phase of the kth subpulse. Fig. 1(b) schematically shows the time–frequency relationships of the OFSL's input and output. As can be seen, the total bandwidth of the generated optical SFC signal is significantly increased compared with the seed light source. Here, it is important to stress that $T_{\mathrm{rp}} \ge N_{\max} T_{\mathrm{L}}$ and $T_{\mathrm{L}} \ge T_{\mathrm{pw}}$ should be satisfied, where T_{rp} is the repetition period of the seed light source, to ensure that there are no residual optical pulse signals in the OFSL before the next optical pulse signal arrives. Besides, a continuous-wave (CW) light (frequency: $f_{\mathrm{cw}} < f_{\mathrm{Lc}}$) phase-locked with the frequency-chirped light is introduced and heterodyned with the optical SFC signal in a photodetector (PD). Therefore, a microwave SFC signal can be produced and expressed as

$$I(t) \propto \sum_{k=0}^{N_{\max}-1} \mathrm{rect}\left(\frac{t-kT_{\mathrm{L}}}{T_{\mathrm{pw}}}\right) \cdot \cos\left\{2\pi\left[f_{ck} + \frac{\gamma(t-kT_{\mathrm{L}})}{2}\right](t-kT_{\mathrm{L}}) + \varphi_k\right\} \quad (2)$$

where $f_{ck} = f_{\mathrm{Lc}} - f_{\mathrm{cw}} + 2(k+1)\Delta f$. After that, the microwave SFC signal is amplified by a power amplifier (PA) and radiated to the free space by a transmit antenna (TA).

The radar echo reflected by the target is collected by a receive antenna (RA) and sent into the receiver, where the radar echo is amplified by a low-noise amplifier (LNA) and fed into the radio frequency (RF) port of a dual-output MZM (DOMZM). Then, the reference signal composed of the optical SFC signal coupled with the CW light is modulated. Assuming that the radar echo is delayed by τ relative to the reference signal and biasing the DOMZM at the quadrature transmission point, the DOMZM will output two optical signals with opposite phases at frequency pairs $\{f_{\mathrm{cw}},\ f_{\mathrm{cw}} + \gamma\tau\}$ and $\{f_{\mathrm{Lc}} + 2(k+1)\Delta f + \gamma(t-kT_{\mathrm{L}}),\ f_{\mathrm{Lc}} + 2(k+1)\Delta f + \gamma(t-kT_{\mathrm{L}} - \tau)\}$. Sending the DOMZM outputs to a narrow bandwidth balanced PD (BPD), a dechirped signal is obtained and written as

$$s(t) \propto \sum_{k=0}^{N_{\max}-1} \mathrm{rect}\left(\frac{t-kT_{\mathrm{L}}-\tau}{T_{\mathrm{pw}}-\tau}\right) \cdot \cos\{2\pi[\gamma\tau(t-kT_{\mathrm{L}}) - \gamma\tau^2/2 + f_{ck}\tau]\}. \quad (3)$$

Due to the low frequency of the dechirped signal, a narrow bandwidth BPD is sufficient to meet the requirements while avoiding high-frequency interference. After converting the dechirped waveform to the digital domain by a low-speed ADC, fast digital signal processing can be implemented in a digital signal processor (DSP) to obtain the target information. For simplicity, (3) only considers one delay, i.e., only one point target in the detection range is considered. However, when there are multiple reflections, the echoes would beat each other to produce unwanted low-frequency signals. Considering that echo powers are usually so small that the beat between echoes produces a negligible signal, thus its influence is ignored here. Furthermore, the balanced dechirping receiver can also be used to eliminate the signal produced by the beat between echoes [20].

B. Compressive Reconstruction of Dechirped Signals

As shown in (3), the dechirped signal is composed of a series of subpulses with discontinuous phases. Thus, coherent processing of these subpulses is necessary to extract precise target information. Introducing time delay $2k\Delta f/\gamma - kT_{\mathrm{L}}$ for each dechirped subpulse, (3) becomes

$$s_{\mathrm{shift}}(t) \propto \sum_{k=0}^{N_{\max}-1} \mathrm{rect}\left(\frac{t-2k\Delta f/\gamma-\tau}{T_{\mathrm{pw}}-\tau}\right) \cdot \cos[2\pi(\gamma\tau t - \gamma\tau^2/2 + f_{c0}\tau)]. \quad (4)$$

From (4), we can see that the subpulses of the dechirped signal can be combined into one synthetic signal without phase discontinuities if $2\Delta f \le B_{\mathrm{L}} - \gamma\tau$ to achieve high-resolution radar detection [39]. The dechirped signal synthesis process is shown in Fig. 2, which shows that the synthetic dechirped signal based on the SFC signal is the same as the signal dechirped from a chirp signal with identical bandwidth. However, the radar in this case is susceptible to interference from other electromagnetic radiators working in the same frequency band. Here, we propose a radar based on an SSFC signal by setting $2\Delta f > B_{\mathrm{L}} - \gamma\tau$ to skip some interference frequency bands, thus improving the anti-interference ability of the radar. On the other hand, there will be some signal gaps in the synthetic signal after the time shift due to the SSFC signal with discontinuous frequency, as shown in Fig. 2(c). Thus, it is necessary to reconstruct the interrupted dechirped signal to achieve high-resolution detection. Here, we introduce a compressive reconstruction of the dechirped signal based on the compressive sensing (CS) theory, which constructs a framework to precisely reconstruct a signal with a sparse or compressible representation [41]. Generally, target echoes

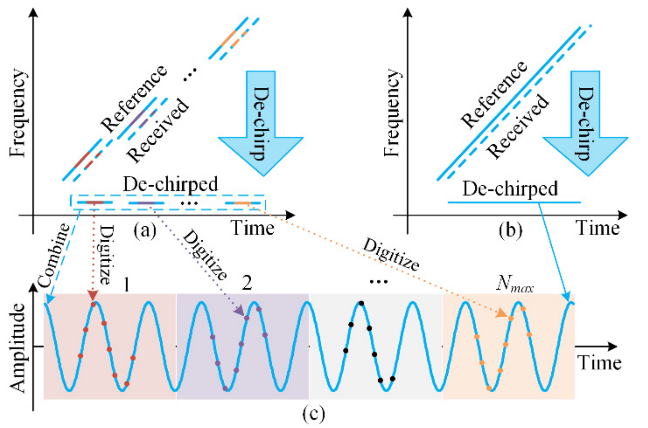

Fig. 2. Illustration of the dechirped signal synthesis and compressive reconstruction concept. (a) and (b) Dechirping processes based on SFC signals and chirp signals, respectively. (c) Dechirped waveform.

can be regarded as the accumulation of that reflected by multiple individual reflectors, especially for high-resolution radars. Therefore, most radar detection scenarios meet the requirement of the CS theory for signal sparsity [42]. In some complex scenes, the hypothesis may not be true, but a suitable basis can be employed to transform the scene to be sparse [43]. In this article, only the simple case is considered.

We first digitize $s_{\mathrm{shift}}(t)$ into an $M \times 1$ matrix as shown by the dot in Fig. 2(c) and denote it as $\mathbf{s}$

$$\mathbf{s} = \boldsymbol{\psi}\boldsymbol{\theta} = \boldsymbol{\psi}\mathbf{W}^{-1}\mathbf{F} = \mathbf{A}\mathbf{F} \tag{5}$$

where $\boldsymbol{\psi}$ represents a measurement matrix of dimension $M \times N$ and $\boldsymbol{\theta} = \mathbf{W}^{-1}\mathbf{F}$ indicates the complete signal we want to reconstruct. $\mathbf{W}^{-1}$ accounts for an inverse discrete Fourier transform (DFT) matrix of dimension $N \times N$, while $\mathbf{F}$ is an $N \times 1$ matrix with DFT values. Moreover, we express $\boldsymbol{\psi}\mathbf{W}^{-1}$ as $\mathbf{A}$ for convenience, which is a partial inverse DFT matrix of dimension $M \times N$. Note that $\mathbf{F}$ is sparse because the radar target can be modeled by a series of multiple scattering centers, in other words, $\boldsymbol{\theta}$ has a sparse representation. According to (5), the high-dimensional signal $\boldsymbol{\theta}$ is projected to the low-dimensional signal $\mathbf{s}$. Therefore, the reconstruction of $\boldsymbol{\theta}$ becomes an ill-posed inverse problem. A variety of well-known methods can be used to solve this problem, but in this work, we reconstruct $\boldsymbol{\theta}$ by solving a minimization problem of l_1

$$\hat{\mathbf{F}} = \arg\min ||\mathbf{F}||_1 \quad \text{s.t.} \quad \mathbf{s} = \mathbf{A}\mathbf{F}. \tag{6}$$

Consequently, the high-dimensional signals $\boldsymbol{\theta}$ can be recovered from the highly incomplete measurements $\mathbf{s}$ by employing the orthogonal matching pursuit (OMP) algorithm [44]. Compared with the dechirped subpulse, the reconstructed dechirped waveform has a longer duration time T, providing an improvement of frequency resolution $\delta f \approx 1/T$ after fast Fourier transform (FFT). As a result, the range resolution δR is increased according to $\delta R = c\delta f/\gamma/2 \approx c/\gamma T/2 = c/2/B$, where c is the microwave propagation velocity and B is the reconstructed bandwidth.

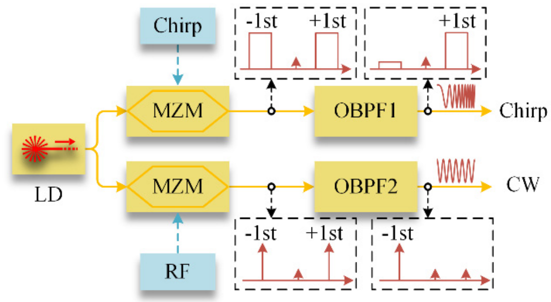

Fig. 3. Experimental setup of the frequency-chirped light and CW light generation.

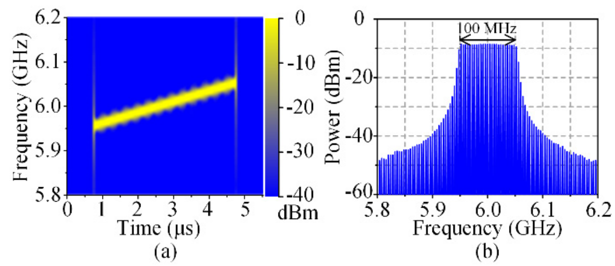

Fig. 4. (a) Time–frequency analysis and (b) spectra of the microwave chirp signal.

III. Experimental Results

A. Experimental Setup

In the experiment, two phase-locked light sources, frequency-chirped light and CW light, were conducted, as shown in Fig. 3. A light with a frequency of 193.403 THz from a narrow linewidth laser diode (LD) is divided into two paths, and each path is sent to an MZM (Fujitsu FTM7938) biased at the null point and followed by an OBPF. The microwave signal modulating the upper path is a 100-MHz bandwidth chirp signal with a center frequency of 6 GHz and the OBPF in the upper path is used to select the +1st-order sideband, while the microwave signal modulating the lower path is a CW signal with a fixed frequency of 10.8 GHz and the OBPF is used to select the −1st-order sideband. Fig. 4(a) and (b) illustrates the time–frequency diagram and the electrical spectrum of the microwave chirp signal. Hence, the upper path produces a frequency-chirped light and the lower path produces a CW light. Excellent frequency sweep linearity of the microwave chirp signal can be easily realized because the desired bandwidth is relatively narrow. Thus, the frequency-chirped light would have sufficient frequency sweep linearity, which depends on the microwave drive signal [45].

In the OFSL, we selected a 200-MHz AOM as the frequency shifter, an erbium-doped fiber amplifier (EDFA) as the OA, a waveshaper as the OBPF, and a 1-km optical fiber to achieve a circulation time of about 5.19 μs. Thus, the frequency of the optical chirp signal is shifted by 400 MHz when the OFSL is open, as shown in Fig. 5(a). It should be noted that the circulation time would be altered by harsh environments, such as platform vibration and temperature drift. Therefore, vibration isolation and thermal control should be

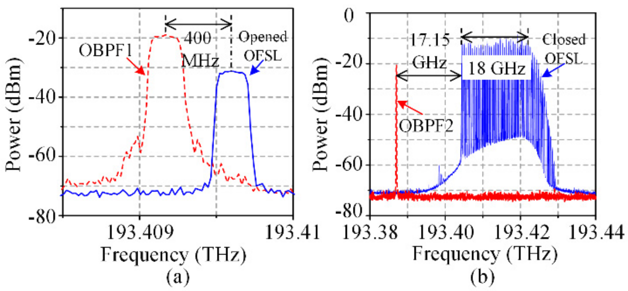

Fig. 5. (a) Output spectra of OBPF1 and the opened OFSL. (b) Output spectra of OBPF2 and the closed OFSL.

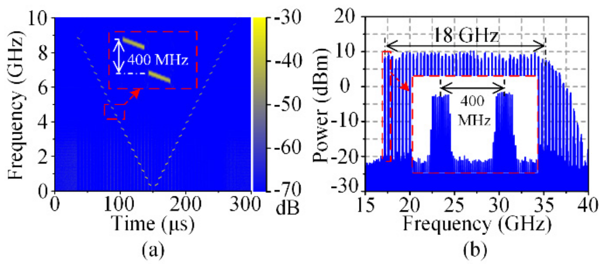

Fig. 6. (a) Time–frequency analysis and (b) spectra of the generated SSFC signal.

implemented to achieve satisfactory performance in practice. However, these actions were not adopted in our experiments considering the relatively stable environment of the laboratory. To close the OFSL and adjust the power gain of the EDFA in addition to the passband frequency of the waveshaper, an optical SFC signal with a bandwidth of about 18 GHz is output from the OFSL, as shown by the blue curve in Fig. 5(b). The optical SFC signal and the CW light are coupled and divided into two portions. One is sent to the receiver as the reference signal, while the other one is sent to a 40-GHz PD to produce a broadband SSFC signal, which is radiated by a TA (16–40 GHz) after being amplified by a microwave amplifier (2–43 GHz). Due to the bandwidth limitation of our oscilloscope, we down-converted the generated SSFC signal to a baseband signal through a mixer before being received by the oscilloscope. Applying the short-time Fourier transform (STFT) to the recorded waveform of the baseband signal, the time–frequency diagram is obtained, as shown in Fig. 6(a). In addition, the spectrum of the SSFC signal is analyzed by an electrical spectrum analyzer, as shown in Fig. 6(b). From that, we can see that the spectrum of the SFC signal is sparse and spans a range of 17.7 GHz (17.15–34.85 GHz), but the actually occupied spectrum is only about 4.5 GHz, which is 25% of the bandwidth (18 GHz) to be reconstructed.

Benefiting from the ultrawide bandwidth, the SSFC signal reflected by the target can carry information with more details. In the receiver, the reflected SFC signal modulates the reference signal from the transmitter through a DOMZM biased at the quadrature point. The outputs of the DOMZM are sent to a 150-MHz BPD to perform dechirping. Afterward, the low-frequency dechirped signal is sampled by an oscilloscope at a sampling rate of 100 MHz and processed in the digital domain with a fast processing speed.

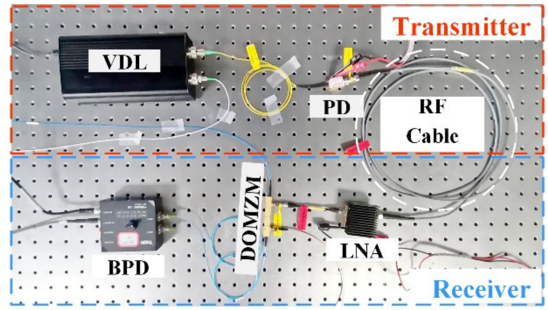

Fig. 7. Experimental setup of the resolution and precision measurement.

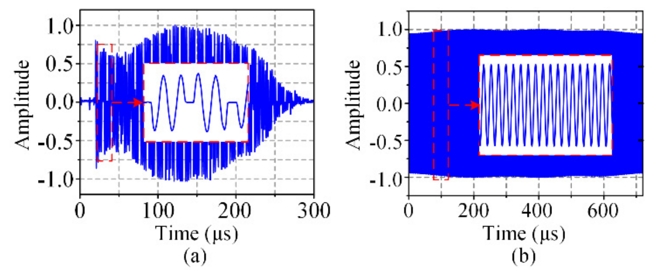

Fig. 8. Normalized waveforms of (a) original dechirped signal and (b) reconstructed dechirped signal.

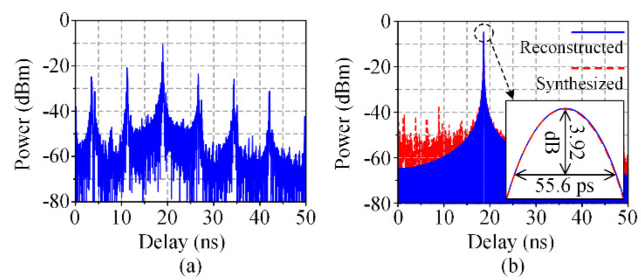

Fig. 9. Delay measurement results based on (a) original dechirped signal and (b) reconstructed dechirped signal and the synthesized dechirped signal.

B. Resolution and Precision Measurement

In this section, we measure the resolution and precision of the proposed system to demonstrate the excellent performance brought by breaking through the bandwidth limitation of electronics. First, an electrical cable links the PD in the transmitter and the LNA in the receiver to emulate a point target while avoiding extraneous interference from the environment. In addition, a variable fiber delay line (VDL) with a typical precision of ±0.01 ps is inserted before the PD in the transmitter. The photograph of the experimental setup is shown in Fig. 7. When the VDL is set at the zero position, the normalized dechirped signal waveform is shown in Fig. 8(a). Delay measurements can be obtained by FFT, but if we employ FFT to the waveform directly, the spectrum will appear with many spurs resulting in misidentification, as shown in Fig. 9(a). To reduce the impact of the high sidelobes on the detection, the normalized dechirped signal is reconstructed, as shown in Fig. 8(b). Performing the FFT on the reconstructed waveform, the result with sufficiently suppressed sidelobes is obtained, as shown by the blue curve in Fig. 9(b). Here, the

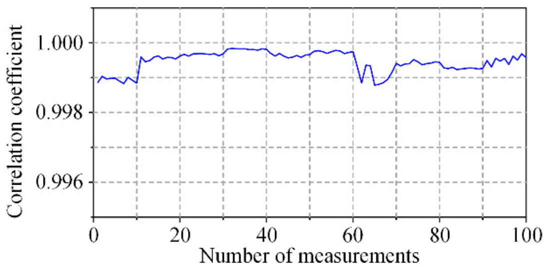

Fig. 10. Average correlation coefficients of 100 measurement results.

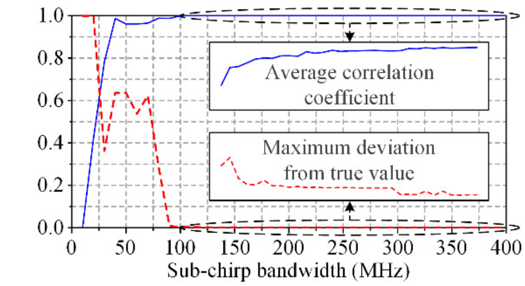

Fig. 11. Results based on different subchirp bandwidths.

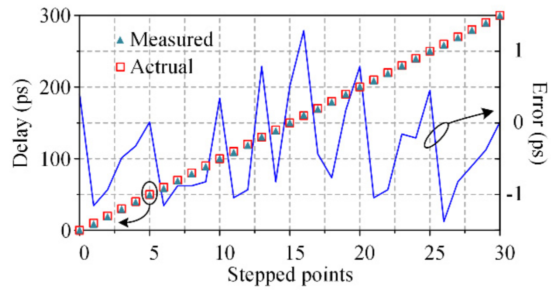

Fig. 12. Comparison of the measured and actual delay.

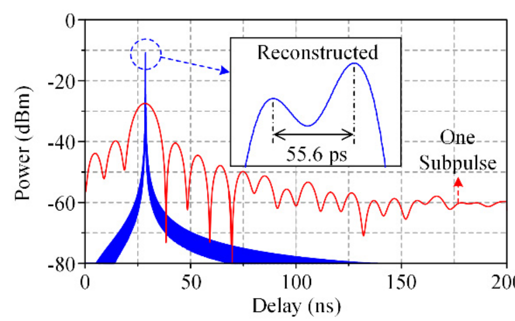

Fig. 13. Results based on one dechirped subpulse and reconstructed dechirped signal.

resolution of the system is verified by measuring the 3.92-dB width $\delta f_{3.92}$ of the main lobe, because $\delta f_{3.92}cT/2B = c/2B$ theoretically [46]. As can be seen from Fig. 9(b), the 3.92-dB width of the main lobe is about 55.6 ps, which means that the minimum range resolution of the radar can reach 8.3 mm. To further verify the correctness of the reconstructed result, the subchirp bandwidth is adjusted to 440 MHz. In this case, the spectrum of the radar signal becomes continuous, so the delay can be obtained by the bandwidth synthesis algorithm [39]. Fig. 9(b) compares the reconstructed and synthesized results. As can be seen, the main lobe positions are almost the same, proving the correctness of the reconstructed results. The correlation coefficient of results based on the reconstruction and the synthesis is calculated to be 0.998. Furthermore, average correlation coefficients are calculated for 100 measurement results, as shown in Fig. 10. It is apparent that the results are all well reconstructed. Although the complete dechirped signal can be recovered by reconstruction, the process of OMP requires additional operations $O(\kappa \log N)$ and takes more time than synthesizing, where κ is the number of scattered points [44]. In the experiment, the average running time on a laptop with AMD Ryzen7 5800H CPU for a dechirped signal reconstruction is 0.15 s, while the synthesizing-based method takes 0.07 s.

Generally, $M > \kappa$ is required to reconstruct the signal. However, it may be less effective when M is too small, i.e., the subchirp bandwidth is too narrow. Thus, we investigated the reconstructed results for different subchirp bandwidths by using part, but not all of the subpulse data dechirped from the SFC signal with a continuous spectrum. The adopted subchirp bandwidth is from 10 to 400 MHz, while the measurement is repeated 100 times every 10 MHz. The average correlation coefficient and the maximum deviation from the true value are, respectively, shown by the blue and red curves in Fig. 11. The average correlation coefficient and the maximum deviation from the true value tend to remain unchanged after 100 MHz. Thus, the subchirp bandwidth is selected as 100 MHz in the following experiments to obtain higher robustness.

We then gradually increase the delay of the VDL from 0 to 300 ps in steps of 10 ps to investigate the detection precision of the proposed system. With a triangle and a rectangle, the measured and actual delays are compared in Fig. 12, providing consistent values. In addition, the statistics for the deviations of detection are displayed by the blue curve in Fig. 12. As can be seen, the deviation is less than ±1.5 ps, meaning that the ranging error is kept within ±225 μm. For comparison, measurements based on the synthesizing method are implemented, obtaining deviations of less than ±0.4 ps. Although the missing signal can be obtained through reconstruction, there are still errors in reconstructing, which increases the detection error.

To further verify the high range resolution of the proposed system, two parallel microwave delay lines with a delay difference of 55 ps are inserted between the PD in the transmitter and the LNA in the receiver. Fig. 13 compares the results obtained from one dechirped subpulse and the reconstructed dechirped signal. In the result obtained from the reconstructed dechirped signal, two peaks are clearly separated, but only one peak is displayed in the result of one dechirped subpulse. The delay of two microwave delay lines is calculated as about 55.6 ps, which is equivalent to a distance of 8.3 mm in space.

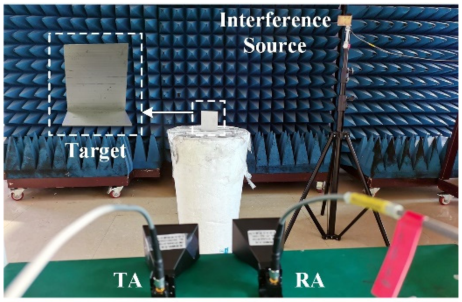

Fig. 14. Photograph of the experimental setup with interference.

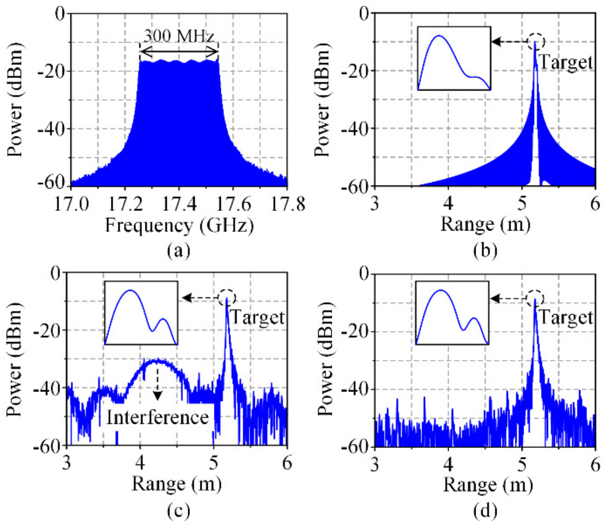

Fig. 15. (a) Interference spectrum. (b) Result obtained by sparse-spectrum radar with interference. (c) and (d) Results obtained by continuous-spectrum radar with and without interference.

C. Radar Detection Experiment

To demonstrate the actual detection performance of the proposed radar, we designed several experiments in real environments. First, a metal plate is detected in an environment full of interference. Interfering signals are radiated through an additional antenna, as shown by the photograph in Fig. 14. The interference spectrum covers from 17.25 to 17.55 GHz, as shown in Fig. 15(a). The interfering spectrum is furnished by a chirp signal with the same chirp rate as the subchirp signal. Due to the employment of the SSFC signal, the proposed radar can avoid using the interfered frequency range to achieve correct detection, as shown in Fig. 15(b), where the peak is split into two due to the high resolution of the radar, in addition, to adjust the subchirp bandwidth to 440 MHz, i.e., the radar operates on a continuous spectrum. In this case, the results of detecting the target with and without interference are shown in Fig. 15(c) and (d). As can be seen, when there is no interference, the radar working with a continuous spectrum can detect the target correctly, but when there is interference, the detection result will generate other interference besides the target. Due to the time of the SSFC signal corresponding to its frequency and the interfering spectrum occupies only a portion of the SSFC spectrum, the duration of the signal generated by the interference signal is shorter than that of the synthesized dechirped signal. Considering that the spectral width is inversely proportional to the signal duration, the interference signal produces a wider spectrum than the synthesized dechirped signal. Thus, the anti-jamming performance of the proposed radar is verified.

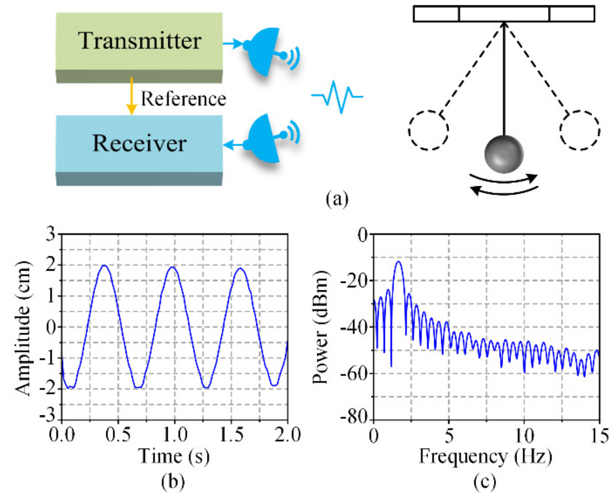

Fig. 16. (a) Experimental setup of the simple pendulum vibration measurement. (b) Measured pendulum trajectory. (c) Spectrum analysis of the trajectory in (b).

Then, a vibration measurement of a simple pendulum in the real environment is conducted to verify the high precision, as shown in Fig. 16(a). The vibration frequency of the simple pendulum can be approximately expressed as

$$f_{\text{vib}} \approx \frac{1}{2\pi\sqrt{l/g}} \tag{7}$$

where l is the pendulum length and g is the gravitational acceleration. In the experiment, the simple pendulum is composed of a wire with a length of about 7.5 cm and a metal ball with a diameter of 3.45 cm. Hence, the theoretical vibration frequency of the metal ball is about 1.653 Hz. The trajectory of the simple pendulum is recorded and displayed in Fig. 16(b). Analyzing the sinusoidal-like trajectory by the FFT, we can obtain a peak close to the theoretical value at 1.649 Hz, validating the ability of the radar to measure the vibration of the target.

The reconstruction scheme employed in this article is to directly reconstruct the dechirped signal. Based on the reconstructed dechirped signal, some mature algorithms, such as the range-doppler (RD) algorithm [47], can be directly used for imaging. Compared with the direct reconstruction of two-dimensional (2-D) images using OMP, the computational complexity is greatly reduced but still maintains a high resolution due to the wide bandwidth. To further verify the system performance, high-resolution 2-D imaging is implemented based on ISAR technologies with the RD algorithm. In addition to the range dimension, the 2-D image has an azimuth dimension, which is perpendicular to the radar line of sight. As shown in Fig. 17(a), five metal corners (size: 1.3 cm $\times$ 1.3 cm $\times$ 1.3 cm), as targets, are placed on a rotating platform with a rotating speed of 360°/s. In this scenario,

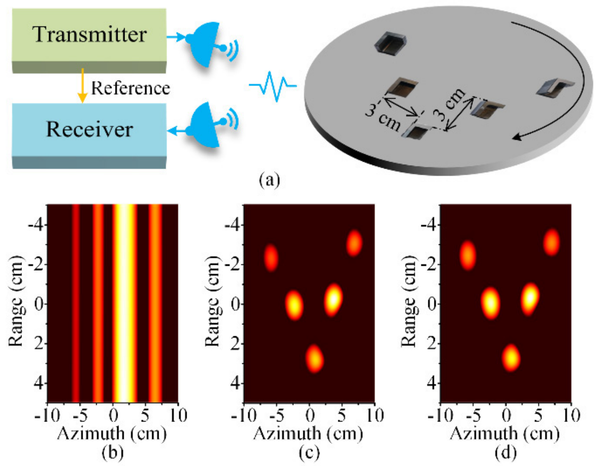

Fig. 17. (a) Experimental setup of the ISAR imaging. (b)–(d) ISAR image based on the original dechirped subpulse, the reconstructed dechirped signal, and the synthetic dechirped signal with an 18-GHz continuous spectrum, respectively.

the azimuth information can be obtained by exploiting the Doppler frequency caused by the rotation. After applying 2-D FFT to reconstructed dechirped signals within the image integration time, range information along with azimuth information can be produced, thereby enabling high-resolution 2-D imaging.

In the experiment, the rotating platform is about 1 m away from radar antennas, and the frequencies of the signal dechirped from target echoes are around 0.37 MHz. Besides, the image integration time is set to 55.6 ms, providing a minimum azimuth resolution of 1.7 cm according to $c/(2\theta F_c)$, where F_c is the center frequency of the SSFC signal and θ is the viewing angle [24]. First, only one of the dechirped subpulses is used to conduct a 2-D ISAR image, as displayed in Fig. 17(b). Due to the low range resolution, five metal corners are failed to be identified. Furthermore, we also conduct a 2-D ISAR image based on the reconstructed dechirped signals, as shown in Fig. 17(c). As can be seen, five points corresponding to five metal corners can be clearly distinguished, demonstrating the excellent performance of the proposed radar. To further verify the feasibility of the proposed approach, we increase the bandwidth of the subchirp signal to 440 MHz, i.e., all the 18 GHz spectrum is occupied. At this time, synthetic dechirped signals are used for imaging instead of compressive reconstructed dechirped signals. The obtained image is shown in Fig. 17(d), which is almost the same as the image obtained using the reconstructed signal.

IV. Discussion

From the above results, we can see that the proposed radar achieves excellent performances of high precision besides high resolution while without the support of broadband electronic ADCs and DACs. Limited by experimental conditions, such as the bandwidth limitations of the PD, antenna, and amplifier, we only demonstrated the working bandwidth of 18 GHz below the Ka-band. The system can achieve better performance by upgrading these devices. For instance, we can expand the bandwidth of the generated SSFC signal by improving the bandwidth of the OBPF in the OFSL. By increasing the frequency difference between the frequency-chirped light and the CW light in addition to adopting a higher frequency PD, the radar could generate a W-band signal with a wide bandwidth, which is currently popular in the field of autonomous driving. It is important to point out that the amplified spontaneous emission (ASE) noise in the OFSL accumulates with the recirculating frequency shift. To evaluate the effect of the ASE noise accumulation on the system, we compared the spectrum of the 1st and 45th dechirped subpulses, as shown in Fig. 18. As can be seen, the spectral floor of the 1st dechirped subpulse is similar to that of the 45th. Thus, the influence of the ASE noise accumulation in the OFSL on the dechirped results can be ignored. However, as the number of frequency shifts increases, the effect of the ASE noise may become apparent. Therefore, the system requires a compromise between the number of frequency shifts and a high signal-to-noise ratio (SNR). Theoretically, as long as the open loop gain of the OFSL is 1, the signal will continue to circulate in the loop if there is no filter in the OFSL. Notwithstanding, the increasing noise in the OFSL may break the balance and limit the number of frequency shifts, but several hundreds of frequency shifts can be provided, as shown in [48] and [49], which is sufficient for microwave applications.

To further investigate the influence of SNR on the dechirped signal reconstruction, simulations under one target scene and different dechirped signal SNRs are carried out. The correlation coefficient between the reconstructed and the real results

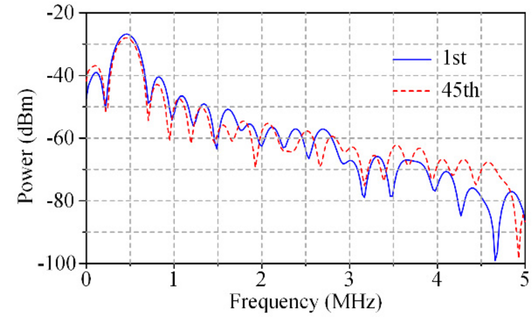

Fig. 18. Spectral comparison of the 1st and 45th dechirped subpulse.

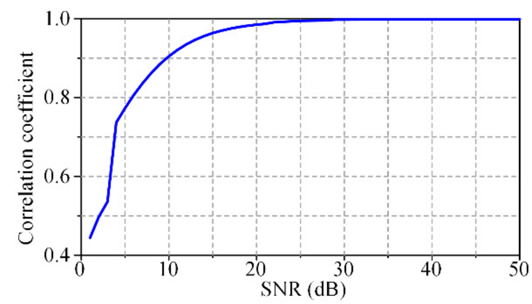

Fig. 19. Correlation coefficient as a function of SNR.

is shown in Fig. 19. When the SNR of the dechirped signal is less than 22 dB, the correlation coefficient increases sharply, while when the SNR of the dechirped signal is greater than 22 dB, the correlation coefficient tends to be stable and close to 1.

Using the signal dechirped from a narrowband chirp signal to simply reconstruct the additional left and right signals may also be possible to achieve effective large-bandwidth and high-range resolution. To compare the reconstruction effect of the two methods, we compared the reconstruction correlation coefficient based on an SSFC signal with the same parameters used in Section III-A and the chirp signal with a bandwidth of 4.5 GHz. The calculated correlation coefficients are 0.998 and 0.930, respectively. Thus, simply reconstructing additional signals left and right of the dechirped signal performs relatively poorly. On the other hand, the chirp signal with continuous spectrum is easier to be intercepted and jammed, while the SSFC signal has better immunity to jamming.

V. Conclusion

In conclusion, we proposed and demonstrated a microwave photonic radar with a sparse spectrum to overcome the bandwidth limitation of conventional microwave radar, so as to achieve high-resolution detection and improve anti-interference ability. The SSFC signal with a wide bandwidth can be produced with a relatively narrowband ESG owing to the help of the OFSL. In addition, the SSFC signal can be fast processed without the demand for high-speed ADC due to microwave photonic dechirping. With the compressive reconstruction of the dechirped signal, the detection resolution and precision are guaranteed. As an application example, we conducted a microwave photonic radar with a sparse spectrum spanning a bandwidth of 18 GHz but only occupying a 4.5-GHz spectrum, achieving almost the same resolution with an 18-GHz continuous spectrum. In the experiment, the system successfully distinguished two simulated point targets with a distance of 8.3 mm and kept the ranging error within $\pm 225\ \mu$m. Moreover, the performance of the proposed radar can be significantly enhanced by upgrading the bandwidth and operating band.

References

[1] Y. Cheng and Y. Liu, "Person reidentification based on automotive radar point clouds," *IEEE Trans. Geosci. Remote Sens.*, vol. 60, pp. 1–13, 2022.

[2] F. Michler, B. Scheiner, T. Reissland, R. Weigel, and A. Koelpin, "Micrometer sensing with microwaves: Precise radar systems for innovative measurement applications," *IEEE J. Microw.*, vol. 1, no. 1, pp. 202–217, Jan. 2021.

[3] F. Scotti, S. Maresca, L. Lembo, G. Serafino, A. Bogoni, and P. Ghelfi, "Widely distributed photonics-based dual-band MIMO radar for harbour surveillance," *IEEE Photon. Technol. Lett.*, vol. 32, no. 17, pp. 1081–1084, Sep. 1, 2020.

[4] B. Zhao *et al.*, "Shallow-layers-detection ice sounding radar for mapping of polar ice sheets," *IEEE Trans. Geosci. Remote Sens.*, vol. 60, pp. 1–10, 2022.

[5] M. Skolnik, *Radar Handbook*, 3rd ed. New York, NY, USA: McGraw-Hill, 2008.

[6] J. Capmany and D. Novak, "Microwave photonics combines two worlds," *Nature Photon.*, vol. 1, no. 6, pp. 319–330, Jun. 2007.

[7] J. Yao, "Microwave photonics," *J. Lightw. Technol.*, vol. 27, no. 3, pp. 314–335, Feb. 1, 2009.

[8] M. Li and N. Zhu, "Recent advances in microwave photonics," *Frontier Optoelectron.*, vol. 9, no. 2, pp. 160–185, Apr. 2016.

[9] J.-M. Wun, C.-C. Wei, J. Chen, C. S. Goh, S. Y. Set, and J.-W. Shi, "Photonic chirped radio-frequency generator with ultra-fast sweeping rate and ultra-wide sweeping range," *Opt. Exp.*, vol. 21, no. 9, pp. 11475–11481, May 2013.

[10] A. Kanno and T. Kawanishi, "Broadband frequency-modulated continuous-wave signal generation by optical modulation technique," *J. Lightw. Technol.*, vol. 32, no. 20, pp. 3566–3572, Oct. 15, 2014.

[11] A. Yacoubian and P. K. Das, "Digital-to-analog conversion using electrooptic modulators," *IEEE Photon. Technol. Lett.*, vol. 15, no. 1, pp. 117–119, Jan. 2003.

[12] T. Hao *et al.*, "Breaking the limitation of mode building time in an optoelectronic oscillator," *Nature Commun.*, vol. 9, no. 1, pp. 1–8, May 2018.

[13] J. Zhang and J. Yao, "Time-stretched sampling of a fast microwave waveform based on the repetitive use of a linearly chirped fiber Bragg grating in a dispersive loop," *Optica*, vol. 1, no. 2, pp. 64–69, Aug. 2014.

[14] H. G. de Chatellus, L. R. Ortés, and J. Azaña, "Optical real-time Fourier transformation with kilohertz resolutions," *Optica*, vol. 3, no. 1, pp. 1–8, Jan. 2016.

[15] Z. Tang, Y. Li, J. Yao, and S. Pan, "Photonics-based microwave frequency mixing: Methodology and applications," *Laser Photon. Rev.*, vol. 14, no. 1, pp. 1–25, Jan. 2020.

[16] T. R. Clark and R. Waterhouse, "Photonics for RF front ends," *IEEE Microw. Mag.*, vol. 12, no. 3, pp. 87–95, May 2011.

[17] G. Serafino *et al.*, "Toward a new generation of radar systems based on microwave photonic technologies," *J. Lightw. Technol.*, vol. 37, no. 2, pp. 643–650, Jan. 15, 2019.

[18] S. Pan and Y. Zhang, "Microwave photonic radars," *J. Lightw. Technol.*, vol. 38, no. 19, pp. 5450–5484, Oct. 1, 2020.

[19] S. Li *et al.*, "Chip-based microwave-photonic radar for high-resolution imaging," *Laser Photon. Rev.*, vol. 14, no. 10, pp. 1–6, Oct. 2020.

[20] X. Ye, F. Zhang, Y. Yang, and S. Pan, "Photonics-based radar with balanced I/Q de-chirping for interference-suppressed high-resolution detection and imaging," *Photon. Res.*, vol. 7, no. 3, pp. 265–272, Mar. 2019.

[21] Y. Li, A. Rashidinejad, J.-M. Wun, D. E. Leaird, J.-W. Shi, and A. M. Weiner, "Photonic generation of W-band arbitrary waveforms with high time-bandwidth products enabling 3.9 mm range resolution," *Optica*, vol. 1, no. 6, pp. 446–454, Dec. 2014.

[22] P. Ghelfi *et al.*, "A fully photonics-based coherent radar system," *Nature*, vol. 507, no. 7492, pp. 341–345, Mar. 2014.

[23] S. Xu, W. Zou, G. Yang, and J. Chen, "Ultra-high range resolution demonstration of a photonics-based microwave radar using a high-repetition-rate mode-locked fiber laser," *Chin. Opt. Lett.*, vol. 16, no. 6, pp. 1–4, Jun. 2018.

[24] F. Z. Zhang, "Photonics-based broadband radar for high-resolution and real-time inverse synthetic aperture imaging," *Opt. Exp.*, vol. 25, no. 14, pp. 16274–16281, Jul. 2017.

[25] R. Li *et al.*, "Demonstration of a microwave photonic synthetic aperture radar based on photonic-assisted signal generation and stretch processing," *Opt. Exp.*, vol. 25, no. 13, pp. 14334–14340, 2017.

[26] A. Wang *et al.*, "Ka-band microwave photonic ultra-wideband imaging radar for capturing quantitative target information," *Opt. Exp.*, vol. 26, no. 16, pp. 20708–20717, Aug. 2018.

[27] Y. Bae, J. Shin, S.-G. Lee, and H. Kim, "Field experiment of photonic radar for low-RCS target detection and high-resolution image acquisition," *IEEE Access*, vol. 9, pp. 63559–63566, 2021.

[28] L. Yang, M. Xing, L. Zhang, G. C. Sun, and Z. Bao, "Integration of rotation estimation and high-order compensation for ultrahigh-resolution microwave photonic ISAR imagery," *IEEE Trans. Geosci. Remote Sens.*, vol. 59, no. 3, pp. 2095–2115, Mar. 2021.

[29] W. Xu, B. Wang, M. Xiang, R. Li, and W. Li, "Image defocus in an airborne UWB VHR microwave photonic SAR: Analysis and compensation," *IEEE Trans. Geosci. Remote Sens.*, vol. 60, pp. 1–18, 2022.

[30] P. Ghelfi, F. Laghezza, F. Scotti, D. Onori, and A. Bogoni, "Photonics for radars operating on multiple coherent bands," *J. Lightw. Technol.*, vol. 34, no. 2, pp. 500–507, Jan. 15, 2016.

[31] S. Wang *et al.*, "Dual-band THz photonic pulses enabling synthetic mm-scale range resolution," *IEEE Photon. Technol. Lett.*, vol. 30, no. 20, pp. 1760–1763, Oct. 15, 2018.

[32] J. Cao *et al.*, "Photonic deramp receiver for dual-band LFM-CW radar," *J. Lightw. Technol.*, vol. 37, no. 10, pp. 2403–2408, May 15, 2019.

[33] S. Peng, S. Li, X. Xue, X. Xiao, D. Wu, and X. Zheng, "A photonics-based coherent dual-band radar for super-resolution range profile," *IEEE Photon. J.*, vol. 11, no. 4, pp. 1–8, Aug. 2019.

[34] Y. G. Lin, B. C. Zhang, Y. Tian, W. Hong, and Y. R. Wu, "Random-frequency SAR imaging based on compressed sensing," *IEEE Trans. Geosci. Remote Sens.*, vol. 34, no. 1, pp. 106–112, Feb. 2013.

[35] W. Li, H. Fan, L. Ren, E. Mao, and Q. Liu, "A high-accuracy phase-derived velocity measurement method for high-speed spatial targets based on stepped-frequency chirp signals," *IEEE Trans. Geosci. Remote Sens.*, vol. 59, no. 3, pp. 1999–2014, Mar. 2021.

[36] F. Zhou, X. Tian, Y. Wang, X. Wang, and X. Bai, "High-resolution ISAR imaging under low SNR with sparse stepped-frequency chirp signals," *IEEE Trans. Geosci. Remote Sens.*, vol. 59, no. 10, pp. 8338–8348, Oct. 2021.

[37] Y. Liu, Z. Zhang, M. Burla, and B. J. Eggleton, "11-GHz-bandwidth photonic radar using MHz electronics," *Laser Photon. Rev.*, vol. 16, no. 4, pp. 1–11, Feb. 2022.

[38] M. A. Richards, *Fundamentals of Radar Signal Processing*, 2nd ed. New York, NY, USA: McGraw-Hill, 2014.

[39] C. Ma *et al.*, "Microwave photonic imaging radar with a sub-centimeter-level resolution," *J. Lightw. Technol.*, vol. 38, no. 18, pp. 4948–4954, Sep. 15, 2020.

[40] C. Ma *et al.*, "Microwave photonic sparse radar with a high range resolution," in *Proc. APCOM YSAOM*, Hong Kong, Feb. 2022, pp. 1–5.

[41] R. G. Baraniuk, "Compressive sensing [lecture notes]," *IEEE Signal Process. Mag.*, vol. 24, no. 4, pp. 118–121, Jul. 2007.

[42] M. T. Alonso, P. López-Dekker, and J. Mallorquí, "A novel strategy for radar imaging based on compressive sensing," *IEEE Trans. Geosci. Remote Sens.*, vol. 48, no. 12, pp. 4285–4295, Dec. 2010.

[43] L. C. Potter, E. Ertin, J. T. Parker, and M. Çetin, "Sparsity and compressed sensing in radar imaging," *Proc. IEEE*, vol. 98, no. 6, pp. 1006–1020, Jun. 2010.

[44] J. Tropp and A. C. Gilbert, "Signal recovery from partial information via orthogonal matching pursuit," *IEEE Trans. Inf. Theory*, vol. 53, no. 12, pp. 4655–4666, Dec. 2007.

[45] Y. Koshikiya, X. Fan, and F. Ito, "Long range and cm-level spatial resolution measurement using coherent optical frequency domain reflectometry with SSB-SC modulator and narrow linewidth fiber laser," *J. Lightw. Technol.*, vol. 26, no. 18, pp. 3287–3294, Sep. 15, 2008.

[46] M. Henri, "The principles of synthetic aperture radar," in *Proc. Synth. Aperture Radar Images*, 2008, pp. 25–55.

[47] V. C. Chen and M. Martorella, *Inverse Synthetic Aperture Radar Imaging: Principles, Algorithms and Applications*. Hertfordshire, U.K.: SciTech, 2014.

[48] H. G. de Chatellus, L. R. Cortés, C. Schnébelin, M. Burla, and J. Azaña, "Reconfigurable photonic generation of broadband chirped waveforms using a single CW laser and low-frequency electronics," *Nature Commun.*, vol. 9, no. 1, pp. 1–12, Jun. 2018.

[49] Y. Lyu, Y. Li, C. Yu, L. Yi, T. Nagatsuma, and Z. Zheng, "Photonic generation of highly-linear ultra-wideband stepped-frequency microwave signals with up to $6{\cdot}10^6$ time-bandwidth product," *J. Lightw. Technol.*, vol. 40, no. 4, pp. 1036–1042, Feb. 15, 2022.